

Alma Mater Studiorum Università di Bologna
Archivio istituzionale della ricerca

Wrinkling poly(trimethylene 2,5-furanoate) free-standing films: Nanostructure formation and physical properties

This is the final peer-reviewed author's accepted manuscript (postprint) of the following publication:

Published Version:

Soccio M., Lotti N., Munari A., Rebollar E., Martinez-Tong D.E. (2020). Wrinkling poly(trimethylene 2,5-furanoate) free-standing films: Nanostructure formation and physical properties. POLYMER, 202, 1-9 [10.1016/j.polymer.2020.122666].

Availability:

This version is available at: <https://hdl.handle.net/11585/763739> since: 2020-07-01

Published:

DOI: <http://doi.org/10.1016/j.polymer.2020.122666>

Terms of use:

Some rights reserved. The terms and conditions for the reuse of this version of the manuscript are specified in the publishing policy. For all terms of use and more information see the publisher's website.

This item was downloaded from IRIS Università di Bologna (<https://cris.unibo.it/>).
When citing, please refer to the published version.

(Article begins on next page)

Wrinkling poly(trimethylene 2,5-furanoate) free-standing films: nanostructure formation and physical properties

Michelina Soccio¹, Nadia Lotti¹, Andrea Munari¹, Esther Rebollar^{2,*}, Daniel E. Martínez-Tong^{3,4,*}

¹Civil, Chemical, Environmental and Materials Engineering Dept., University of Bologna, Via Terracini 28, 40131, Bologna, Italy

²Instituto de Química Física Rocasolano (IQFR-CSIC), C/Serrano 119, 28006, Madrid, Spain

³Departamento de Física de Materiales. Basque Country University (UPV/EHU). Apdo 1072. 20080, Donostia, Spain.

⁴Centro de Física de Materiales (CSIC-UPV/EHU). P. Manuel Lardizabal 5. 20018, Donostia, Spain.

Corresponding authors: e.rebollar@csic.es

danielenrique.martinez@ehu.eus

Abstract

Polymer nanostructures were developed on fully bio-based poly(trimethylene furanoate) (PTF) films, by using the technique of Laser Induced Periodic Surface Structures (LIPSS). We found that irradiation times between 1 – 8 min allowed the formation of periodic and nanometric ripples, when using an UV pulsed laser source at a fluence of 8 mJ/cm². The wrinkled surfaces were studied by a combined macro- and nanoscale approach. We evaluated possible physicochemical changes taking place on the polymer surface after irradiation by infrared spectroscopy, contact angle measurements and atomic force microscopy. The macroscopic properties of PTF showed almost no changes after nanostructure formation, differently from the results previously found for the terephthalic counterparts, as poly(ethyleneterephthalate), PET, and poly(trimethyleneterephthalate), PTT. At the nanoscale, the surface mechanical properties of the nanostructured PTF were found to be improved, as evidenced by force spectroscopy measurements. In particular, an increased Young's modulus and higher stiffness for the nanostructured sample were measured.

1. Introduction

The synthesis and growth of polymer nanostructures have gained important interest during the past decade due to their enhanced physical and chemical properties, as well as for their potential applications, as carefully reported in recent reviews [1-5]. However, in order to implement the use of these nanomaterials into high throughput industrial processes in the plastics sector, several conditions must be accomplished. For example, the formation of the nanostructures must be able to be carried out in a fast and reliable way, without the requirement of particular conditions as clean rooms, high vacuum, or complex mask fabrication. The technique of Laser induced Periodic Surface Structures (LIPSS) fulfills these requirements [1, 6-8]. The formation of LIPSS results from the illumination of the material using a linearly polarized laser beam and gives rise to the spontaneous growth of surface nanostructures with a periodicity which may be described by the expression $\Lambda = \lambda / (n_{\text{ef}} \pm \sin \theta)$, where λ is the laser wavelength, n_{ef} is the effective refractive index at the surface of the material and θ is the angle of incidence of the laser [9]. Thus, the period is close to the wavelength of the laser beam (100 nm – 1 μm) when irradiation takes place at normal incidence ($\Lambda = \lambda / n_{\text{ef}}$). The complete experimental procedure is carried out in ambient conditions, without the use of masks and/or stamps, the irradiation time is in the order of minutes, and the energy of the laser pulses is well below the ablation threshold of the material. The formation of LIPSS in polymers has been widely reported in the literature [6, 10-18]. These nanostructured materials have found applications in several topics, as cell adhesion and growth [19, 20], Surface Enhanced Raman Scattering (SERS) sensors [6, 21, 22], and electrical devices of polymer surfaces for organic electronics [6, 23, 24].

Considering the current demand for plastics having a low environmental impact, but showing at the same time outstanding solid-state properties, an important *hot topic* for

research is centered on the production and application of bio-based polymers [25]. In particular, we highlight the positive impact of polymers based on the 2,5-furandicarboxylic acid (2,5-FDCA) [26, 27]. 2,5-FDCA is considered the “building block of the future”, being obtainable from biomass throughout a process with almost negligible environmental impact [28]. Besides being a 100% green monomer, 2,5-FDCA allows the obtainment of high-performance plastics from the thermal, mechanical and barrier properties point of view, being even better than their terephthalic counterparts [29-31]. From the chemical point of view, both furan dicarboxylic and terephthalic acid moieties contain an aromatic ring responsible for the very good functional properties. Poly(ethylene furanoate) (PEF) is the most important and studied furan-based polyester, and it is the most credible alternative to PET. The outstanding properties of PEF allow the fabrication of films and fibers, and it is currently proposed for packaging of soft drinks, alcoholic beverages, and mineral water [32, 33]. More recently, both academic and industrial interest has focused on another member of the furan-based polyesters, poly(trimethylene furanoate) (PTF). The thermal, mechanical and barrier properties of compression-molded PTF films have been deeply investigated [34-36]. PTF has shown mechanical features similar to those of PEF, resulting even in a better performance from the gas barrier properties point of view [34, 35]. Such exceptional properties render it as an excellent candidate not only for food packaging applications but also for other possible fields, as sensors and electronics, in which a superior capability of blocking the gas molecules flow is required.

In this view, in the present paper, we report the formation and physicochemical properties of LIPSS on fully bio-based, and free-standing, PTF films. We evaluated the nanostructure assembly as a function of irradiation time, and studied the possible changes suffered by the polymer after irradiation. Nanomechanical measurements allowed

quantifying an enhancement of the surface mechanical properties of PTF after nanostructure development. Our findings were discussed taking into consideration the chemical characteristics of the PTF, and have been compared with the results obtained previously on terephthalic-based counterparts, such as PET and PTT.

2. Experimental section

Materials. 2,5-furandicarboxylic acid 98% (2,5-FDCA) (CHEMOS GmbH & Co. K), 1,3-propanediol (PD) and antimony trioxide (Sb_2O_3) (Sigma Aldrich) were reagent grade products.

Synthesis. Poly(trimethylene 2,5-furanoate) (PTF) was synthesized according to the well-known two-step polycondensation process, starting from 2,5-FDCA (5 g) and PD (17 g), and Sb_2O_3 (20 mg), this last being the catalyst of the polymerization process. The reagents together with the catalyst were charged in a thermostated and mechanically stirred glass reactor. The first stage was carried out at 180 °C in nitrogen atmosphere for 2 hours. In the second phase, the temperature was gradually raised till 220 °C and the pressure regularly reduced to 0.1 mbar. These conditions have been kept till a constant value of torque was recorded (2 hours).

Molecular characterization. Proton nuclear magnetic resonance spectroscopy (^1H -NMR, Varian Inova 400-MHz Instrument, Agilent Technologies) was employed to determine the structure. The molecular weight of PTF was obtained by means of gel permeation chromatography (GPC) at 30°C using a 1100 HPLC system (Agilent Technologies), equipped with PLgel 5-mm MiniMIX-C column and UV index detector. A mixture of chloroform/hexafluoro-2-propanol (95/5 v/v) was used as eluent (0.3 mL/min). A calibration curve was obtained using monodisperse polystyrene standards in the range of 800 – 100000 Da.

Film preparation. Free-standing films have been prepared by compression moulding the as-obtained polymer into two Teflon plates at 200 °C under a pressure of 2 ton/m² (Carver C12 press). The obtained PTF free-standing films had a thickness of about 140 ± 5 µm.

Laser induced periodic surface structures (LIPSS). LIPSS were developed using a linearly polarized laser beam from a Q-Switched Nd:YAG system (Lotis TII LS-2131M). We used a wavelength corresponding to the fourth harmonic of the fundamental ($\lambda = 266$ nm) since PTF absorbs efficiently at this wavelength. The pulse duration was 8 ns, and the repetition rate was 10 Hz. Irradiation experiments were performed in ambient air, at normal incidence, and a fluence of 8 mJ/cm², chosen on the basis of laser fluences used for similar polymers [37]. Fluence was calculated measuring the energy in front of the polymer sample and considering a laser spot with a diameter of 5 mm. The effect of the number of pulses was studied.

Physicochemical studies. Differential Scanning Calorimetry (DSC) measurements were carried out in a TA Instruments Q2000, with a liquid nitrogen cooling system, using a ramp of 3 K/min. Samples for DSC experiments were prepared by encapsulating about 5 mg of PTF in aluminum pans. The glass transition temperature (T_g) was taken as the mid-value of the calorimetric step. The cold crystallization (T_{CC}) and melting (T_m) temperatures were calculated as the onset of the peaks.

Fourier Transform Infrared Spectroscopy (ATR-FTIR) measurements were performed at room temperature on a Jasco 3600 FTIR spectrometer, in the ATR geometry.

Contact angle (CA) measurements were performed on irradiated and non-irradiated PTF films. We used a pocket goniometer PG2 (FIBRO system). The static wetting CA was measured at room temperature and ambient humidity using deionized water, paraffin oil and glycerol (Sigma-Aldrich) as liquid probes. A statistical analysis to obtain each CA

value was carried out, performing eight measurements per sample. The surface free energy components were calculated from the measured CA values.

Nanoscale study. Atomic Force Microscopy (AFM) experiments were carried out using a Multimode AFM equipped with a Nanoscope V controller (Bruker, Nanoscope 8.15 - Build R3Sr8.103795). We characterized the surface topography of the samples via tapping mode measurements. We used Tap300Al-G probes, by BudgetSensors, with a usual resonance frequency (f_0) of ~ 250 kHz.

The nanomechanical properties were also studied by means of AFM. For mechanical mapping, we used the PeakForce-Quantitative Nanomechanical Mapping (PF-QNM) protocol. This approach has been used extensively in recent literature to evaluate nanomechanical contrast in polymer systems [38-41]. PF-QNM allows the simultaneous mapping of topographical and nanomechanical features, being the latter related to the surface elastic modulus, tip-sample adhesion force and surface deformation. Briefly, in this operation method the probe performs force-distance curves on each pixel, at a 2 kHz sinusoidal modulation frequency (f_m). For PF-QNM measurements, we also used Tap300Al-G probes. The ratio between f_m/f_0 was in the 120 – 180 range. This indicates that the probe-system conditions were adequate for proper mechanical moduli quantification via nanomechanical mapping, as discussed in Ref [42]. The cantilever spring constant was calculated using the Sader method [43] and found to be 20 N/m. The tip radius was calculated using a PET standard as detailed in the following paragraph. During imaging, we captured 256x256 resolution nanomechanical maps, at a Peak Force setpoint of 50 nN. Tapping images and PF-QNM maps were analyzed using the Nanoscope Analysis 1.90 software (Bruker).

Based on the PF-QNM maps, on fixed zones of the samples' surfaces we performed force spectroscopy measurements. In force spectroscopy, the cantilever approaches, “pokes

into” the sample, and then withdraws, following a linear displacement. During this measurement, the cantilever deflection vs. piezo movement (*Z* direction) is measured, and this can ultimately be converted to a force vs. tip-sample separation plot that provides mechanical information about the sample. All of our force spectroscopy measurements were carried using a *Z* ramp of 200 nm, at a rate of 1 Hz, and collecting 9728 samples. The maximum applied force was 60 nN. For analysis of the force spectroscopy curves, we used a tip radius value of 35 nm. We found this value by fitting a force-distance curve performed on a free-standing PET film (provided by GoodFellow, thickness ~200 μm) to the DMT model (eqn (1), as described below). We fixed the Young’s modulus of PET to be 1.6 GPa, as reported in the literature [39], and left the rest of the fitting parameters *free*, allowing obtaining the above-mentioned radius. Further details are available in the Supporting Information file. All force spectroscopy results were analyzed using self-developed fitting tools.

3. Results and Discussion

3.1. Molecular and thermal characterization

The chemical structure of PTF (Figure 1 inset) has been verified by ^1H -NMR: we can observe the singlet of -C-H of furan ring at 7.30 ppm, the triplet of -CH₂-O- at 4.55 ppm and the multiplet of -CH₂- at 2.30 ppm. The corresponding molecular weight was 31000 Da with a polydispersity index of 2.2.

Figure 1 shows the DSC results for the PTF free-standing film. The film was cooled from room temperature down to -50 °C and the calorimetry measurements were performed on heating, to preserve the thermal history of the film. We observed three calorimetric signals: the endothermic step corresponding to the glass to rubber transition, an exothermic peak related to cold crystallization, and an endothermic signal associated to

the melting of PTF crystals developed during the heating scan. The quantitative values of the above described phenomena are summarized in Table 1. From those results, we concluded that the *as-casted* PTF free-standing films are amorphous and in the glassy state prior irradiation, being T_g located above room temperature and $\Delta H_{CC} = \Delta H_m$.

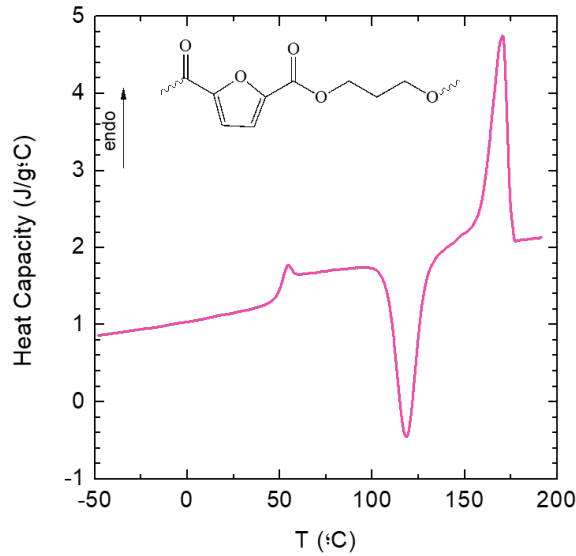


Figure 1. DSC trace of the *as-casted* PTF free-standing film. Inset shows the PTF chemical formula.

Table 1. Thermal characterization data of the PTF free-standing film

	T_g (°C)	ΔC_p (J/g°C)	T_{CC} (°C)	ΔH_{CC} (J/g)	T_m (°C)	ΔH_m (J/g)
PTF	52	0.34	108	31	158	32

3.2. Wrinkle formation by LIPSS

Figure 2 shows $5 \times 5 \mu m^2$ AFM topography images of PTF films after different irradiation times, as described above. The Figures' labels correspond to the number of pulses; the higher this value, the longer the irradiation time. In addition, each Figure is accompanied by a corresponding height profile, taken perpendicularly to the ripples. The non-irradiated

PTF film (0p) showed a continuous surface topography. As expected from the DSC measurements, there are no topographical indications of crystalline structures. The sample had a mean roughness value of 43 nm, as quantified from the AFM height image. This value is about 10 times higher than those previously reported by some of us for PET and PTT free-standing films, prior laser irradiation [37, 44].

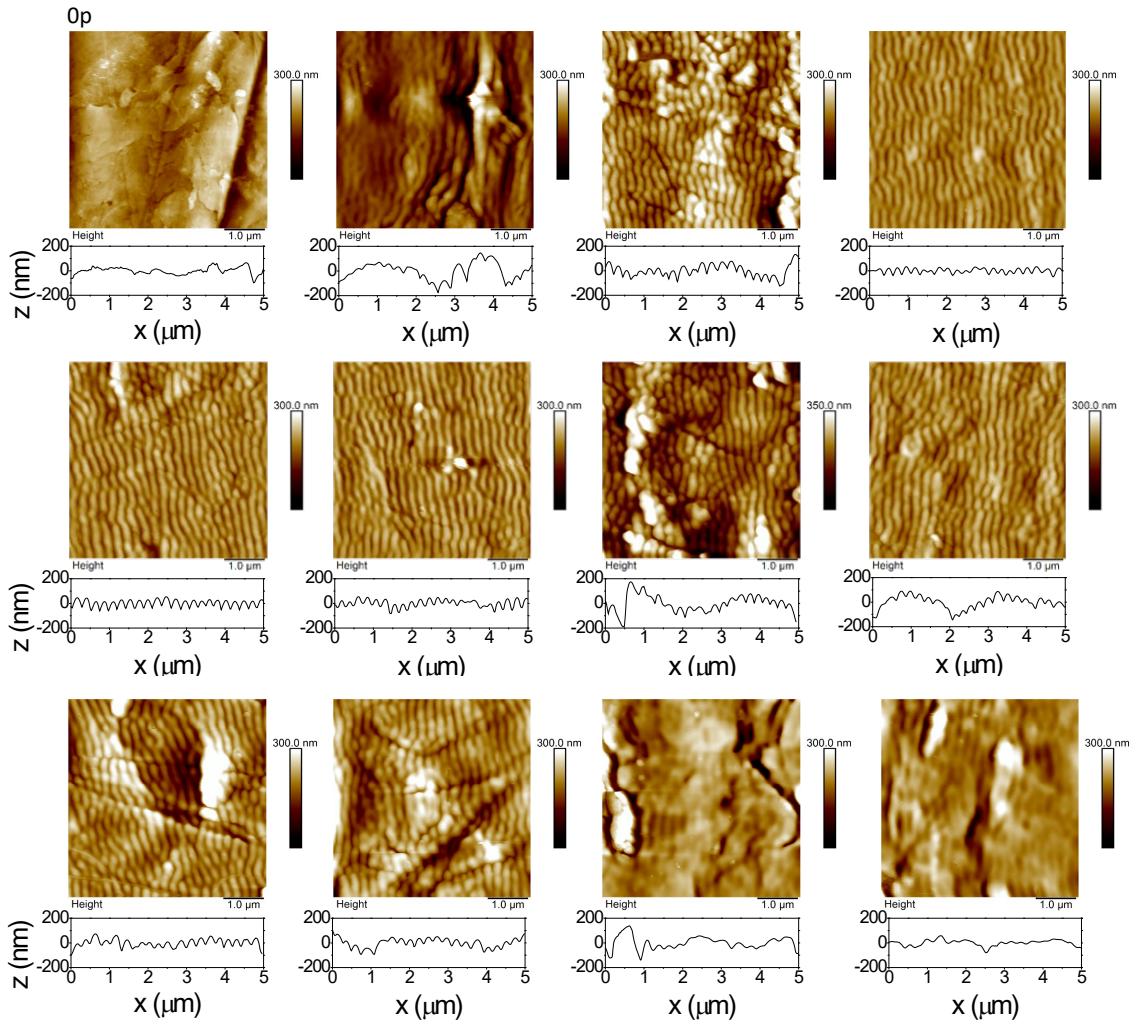


Figure 2. AFM topography images of non-irradiated (0p) and irradiated PTF films.

In order to form LIPSS, it is necessary to irradiate with a few hundreds of pulses. After every single pulse the material is heated and cooled down, and to form wrinkles, the surface temperature must overcome T_g . This allows polymer segmental and chain

dynamics. The heating above T_g is expected to induce an increase of surface roughness caused by capillary waves, thus enhancing surface inhomogeneities and facilitating the feedback mechanism involved in LIPSS formation [6]. In Figure 2, we observed the formation of a wrinkled surface, composed by periodic nanostructures, after irradiation for 300 pulses. This last value was similar to those found for the formation of LIPSS on PET at comparable irradiation conditions [39, 44]. However, by comparing with the formation of LIPSS on the specific PTF terephthalic counterpart, *i.e.* PTT, we noticed several differences. As reported by Rodríguez-Beltrán and collaborators [37], using the same fluence (8 mJ/cm^2) and an even higher number of pulses (3000p), there was not a good formation of LIPSS on a PTT free-standing film yet.

To overcome this issue, authors had to increase the fluence by 25%, up to 10 mJ/cm^2 , for the same high number of pulses [37]. Considering the chemical structure of both PTF and PTT, in principle, this evidence points out towards the positive role the furanic ring has on LIPSS formation. In other words, it seems that the furan-based polymer has a more efficient LIPSS formation capability, compared with the terephthalic one. Also, we highlight that if one considers the high roughness of the PTF surface, it is quite interesting the possibility of structuring it at a relatively low number of pulses.

By increasing the number of pulses, we observed better-defined LIPSS on the PTF surface (Figure 2). The AFM images indicated that the upper limit of pulses dose is above 5400p. In fact, samples irradiated with 6600p and 7200p showed the disappearance of the ripple morphology, indicating that the irradiation dose is too high and that probably some melting is occurring. To provide quantitative values to account for LIPSS formation on PTF, we analyzed the AFM height images to obtain the geometrical characteristics of the wrinkled surfaces (period and depth of the ripples), as a function of the number of pulses. These results are presented in Figure 3. Specifically, Figure 3(a) shows that the

nanostuctures period remains almost constant throughout the whole range of pulses. We found a mean value of 230 ± 10 nm in the 300p – 5400p range, a value fairly close to the laser wavelength, as expected [1, 6]. The longest irradiation times, 6600p and 7200p, showed an increase in the period due to the merging of the structures as a consequence of too high irradiation dose. Figure 3(b) shows the depth of the nanostructures as a function of pulses. We observed that for the shorter irradiation time, the depth of ripples reaches only about 10 nm. Then, in the 600p – 4800p range, the depth showed a constant value of 50 ± 20 nm. The observed increase can be explained because the depth heated by laser irradiation increases with the irradiation time, due to the positive feedback mechanism mentioned above. Finally, around and above 5400p, the depth decreased monotonically. This is related to the results previously observed for the period dependence, since for this high number of pulses the structures start to merge and material melts, making the structures less pronounced. For an even higher number of pulses material will be ablated/removed. Both the period and depth of the LIPSS formed on PTF films are in good agreement to those previously found for PET [39, 44] and PTT [11, 37]. Our results allow concluding that, at a fluence of 8 mJ/cm^2 and using an UV laser source, the 600p – 4800p range is the best one for the formation of LIPSS on PTF.

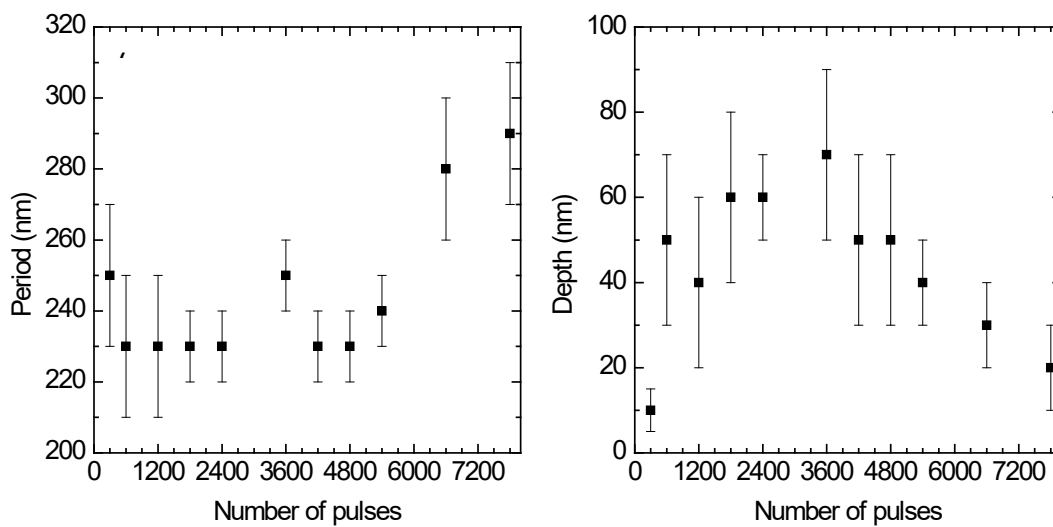


Figure 3. Period (a) and depth (b) of PTF LIPSS, as a function of the number of pulses.

3.3. Physicochemical properties of nanostructured films

To evaluate the physicochemical properties of the wrinkled PTF, we focused on the sample prepared using 3600p, from now on called PTF-LIPSS. We combined macroscopic and nanometric measurements, to allow us probing the overall response of the nanostructures, as well as the possible individual changes.

Starting with the macroscopic measurements, Figure 4 shows the ATR-FTIR results for our samples. The dashed line corresponds to the PTF film (non-irradiated), while the continuous line shows the spectrum of PTF-LIPSS. We observed that both spectra superimposed each other mostly. We only observed the formation of a shoulder around 1600 cm^{-1} for the PTF-LIPSS sample. Signals around this value are usually related to C=O bands. Above 3000 cm^{-1} the PTF-LIPSS spectrum showed a broad peak. Bands around 3500 cm^{-1} are usually assigned to -OH groups and are used as an indication of surrounding humidity. We can discard this latter fact because, if so, both samples should have presented the same behavior. Then, the ATR-FTIR results indicate that there are some chemical modifications taking place after laser irradiation of the PTF, where -OH and/or -COOH groups are introduced. Similar results have been reported in the case of PET [45], where an increase of -COOH groups has been observed after UV irradiation, their formation following a similar pattern to that obtained in its photochemical degradation (Norrish type photofragmentation) for the follow-up reactions after primary radical formation, or by a Norrish-like thermal pathway.

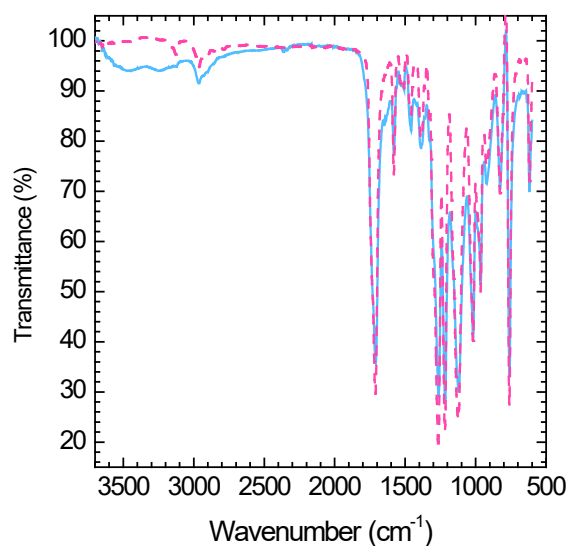


Figure 4. ATR-FTIR spectra of PTF (dashed line) and PTF-LIPSS (continuous line).

To identify further macroscopic changes in the physicochemical properties, Figure 5 shows the CA experiments for both PTF and PTF-LIPSS. In this Figure, we present the images of water, glycerol, and paraffin oil drops on both surfaces. Measurements were performed 24 h after irradiation. The measured mean CA values are reported in Table 2.

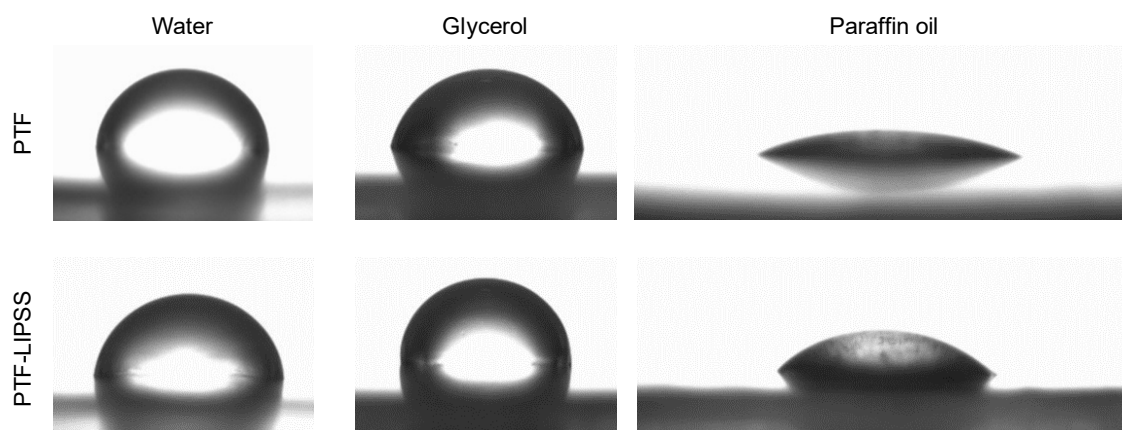


Figure 5. Images of a drop of different liquids on the surface of PTF and PTF-LIPSS.

Table 2. Contact angle measurements and surface energy results for PTF and PTF-LIPSS. Contact angle values (θ) are the mean and standard deviation. Surface free energy

components were calculated as stated in the manuscript. Error value were found by propagation.

	$\theta_{\text{WATER}} (^{\circ})$	$\theta_{\text{GLYCEROL}} (^{\circ})$	$\theta_{\text{PARAFFIN}} (^{\circ})$	$\gamma^{\text{d}}_{\text{S}}$ (mJ/m ²)	$\gamma^{\text{p}}_{\text{S}}$ (mJ/m ²)	γ^{TOTAL} (mJ/m ²)
PTF	82 ± 1	80 ± 2	26 ± 4	50 ± 10	10 ± 4	60 ± 14
PTF-LIPSS	79 ± 2	82 ± 3	48 ± 6	40 ± 10	17 ± 7	57 ± 17

In the case of water, the PTF film showed a slightly hydrophilic behavior ($\theta_{\text{WATER}} < 90^{\circ}$, Table 2). After irradiation, we observed a small decrease in θ_{WATER} ($\sim 4\%$). In previous works dealing with LIPSS on free-standing films of PET and PTT [20, 37, 44], the authors observed higher decrease of water CA value for the irradiated samples, of about 30% and 60% for PET and PTT, respectively. Considering that the water CA decrease can be related to polar functional groups produced on the polymer surface by oxidation process occurring during irradiation, our θ_{WATER} results might indicate that the PTF suffers just a slight surface oxidation, in agreement with the ATR-FTIR results. We found similar evidences when the CA was probed using glycerol, the other polar liquid. In this case, for the PTF film, we measured a $\theta_{\text{GLYCEROL}} = 80^{\circ}$. This value did not change after the film was irradiated. Finally, the CA measurements with the non-polar paraffin oil liquid presented different results. In this case, we observed a significant increase in the CA value, from 26° to 48° , after irradiation. Again, this effect **could** be explained based on an increase of polar groups on the polymer surface that reduce the affinity with the non-polar paraffin oil used for the measurement. This result agrees well with the observations by ATR-FTIR, where the PTF-LIPSS sample showed a broad peak in the -OH region.

We also need to consider the differences in roughness for both samples, since this parameter has an effect on wettability. If we consider a homogeneous wetting model as Wenzel's model [46], the contact between the liquid and the surface of the sample is not

altered by the presence of air and the variation of the contact angle is explained as a function of a parameter called r . This parameter is given by the relation between the total surface of solid in the solid-liquid interface, and the projection of the total surface of solid in the interface, as $r = (\text{total surface})/(\text{projected surface})$. Then, the contact angle of the rough surface (θ^*) would follow: $\cos\theta^* = r \cos\theta$. Therefore, when r increases, if the original sample was hydrophilic it will become more hydrophilic, and if it was hydrophobic it will become more hydrophobic.

Wenzel's model could explain the behavior observed for the water contact angle, but not for the rest of liquids. We then need to consider the Cassie-Baxter model [47], which considers that for rough materials the liquid does not penetrate the grooves on rough surface and leaves air gaps. In this case, $\cos\theta^* = f_s \cos\theta_s + f_v \cos\theta_v$, where f_s and f_v stand for fraction of the solid and vapor on the surface while θ_s and θ_v refer to the intrinsic contact angle on the original smooth surface, and $\theta_v = 180^\circ$ (implying that a suspended liquid droplet in air is a perfect sphere). In this way the equation can be rewritten as follows:

$$\cos\theta^* = f_s(\cos\theta_s + 1) - 1.$$

If we consider a change in the fraction of the solid at the surface, with a value of 0.9, contact angle obtained for water would be 88° , for glycerol 86° and for paraffin 44° . These values are close to the ones obtained experimentally. For water and glycerol, the experimental values are smaller than these ones, which can indicate the role of the chemical modifications.

From the CA results, we calculated the surface free energy components of the polymer films. We used the Owens, Wendt, Rabel and Kaelble (OWRK) model [48, 49]. The OWRK model requires the CA values of the three liquids probed, and uses the Young's equation to determine the total surface energy (γ_{TOTAL}), and the dispersive (γ^d_s) and polar (γ^p_s) components of the surface tension. The components of the surface free energy of the

liquids were found in Ref [50]. The results for the calculated total surface energy, and its components, are summarized in Table 2. We observed no change, above experimental error, in the values of the total surface energy of PTF and PTF-LIPSS. This result is opposite to the observations on PET and PTT [20, 37, 44]. In these works, authors observed an increase of the total surface energy in the irradiated samples, indicating changes in the surface physicochemical properties.

Thus, combining ATR-FTIR and CA results, we can conclude that the formation of LIPSS in PTF does not involve important physicochemical changes in the material. This is a very important and interesting result, since it shows that laser irradiation of PTF allows the formation of a wrinkled surface with periodic nanostructures, without changes in the material's properties, contrary to what has been observed for the terephthalic counterparts.

3.4. Nanomechanical response of nanostructured films

Now, we turn the attention to a nanometric analysis of the samples. The idea was to obtain information about possible changes in a “*ripple-by-ripple*” fashion. To achieve this goal, we performed two complementary measurements. First, we performed a nanomechanical mapping on the polymers' surfaces using the PF-QNM method, to evaluate possible areas with interesting mechanical contrast. Then, on selected zones of the materials, we performed force spectroscopy measurements.

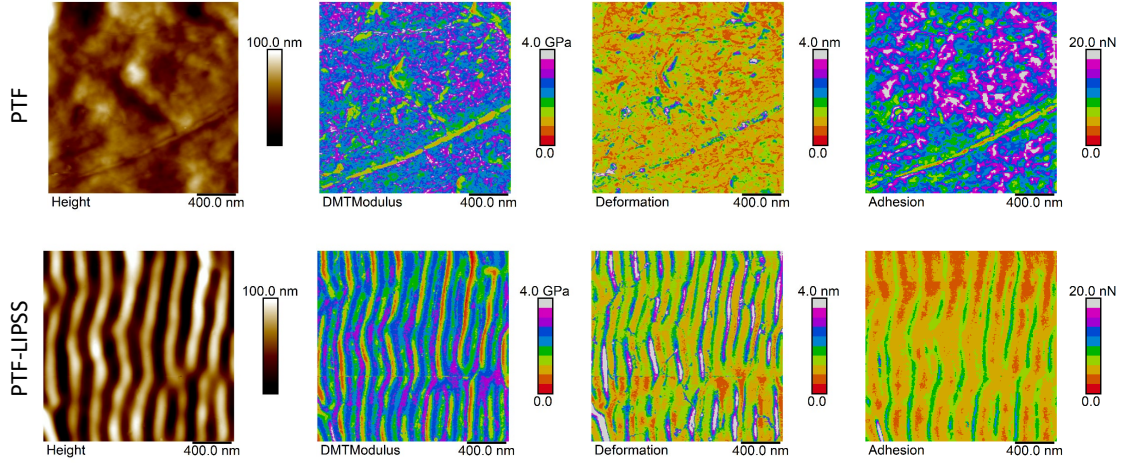


Figure 6. PF-QNM maps of PTF (top row) and PTF-LIPSS (bottom row).

Figure 6 shows the PF-QNM nanomechanical maps for both samples. The PTF film (top row) showed continuous maps with a randomly distributed mechanical contrast in all the evaluated physical properties. This indicates a mechanical homogeneity of PTF, *i.e.*, there are not any particular zones showing distinct mechanical properties, as expected. The PTF-LIPSS film (bottom row in Figure 6) presented nanomechanical maps with a sort of modulation. The variations in the mechanical properties were coupled to the ripples' topography. For example, mechanical modulus maps of PTF-LIPSS showed the same constant value for both top and bottom of the ripples, and variations at the ripples' sides. This trend was also observed for the rest of the properties (deformation and adhesion maps). The origin of the observed nanomechanical contrast relates in principle to the shape and aspect ratio of the LIPSS, compared to the AFM tip radius. In detail, at the bottom and top of the ripples, the sample surface curvature can be considered as flat compared to the tip radius, as previously discussed [39]. Nonetheless, when probing the nanostructures' sides the curvature condition does not hold anymore and, thus, one could calculate unreliable values. As a first quantitative analysis, we compared the mean values of the nanomechanical maps, between the PTF and PTF-LIPSS. We observed an almost

invariable mechanical modulus (~ 2.5 GPa), and deformation (~ 1 nm) for both cases. However, we observed differences in the adhesion maps. In particular, the PTF-LIPSS showed a reduction in adhesion, from 13 to 5 nN. This result is in line with previous reports on PF-QNM studies of LIPSS on PET and other polymeric materials [6, 39].

To enhance our nanomechanical study, we performed force spectroscopy measurements on selected zones of our samples. In this case, the probe was positioned onto different spots of interest, and force-separation curves were recorded. This allowed avoiding the possible artifacts introduced by the dynamic nature of PF-QNM mapping. In Figure 7, we present examples of usual force-separation curves for three different cases, namely, non-irradiated PTF, PTF-LIPSS at the top of the ripples, and PTF-LIPSS at the bottom of the ripples. We explicitly avoided probing the LIPSS sides to focus only on areas that could be considered flat, compared to the tip radius.

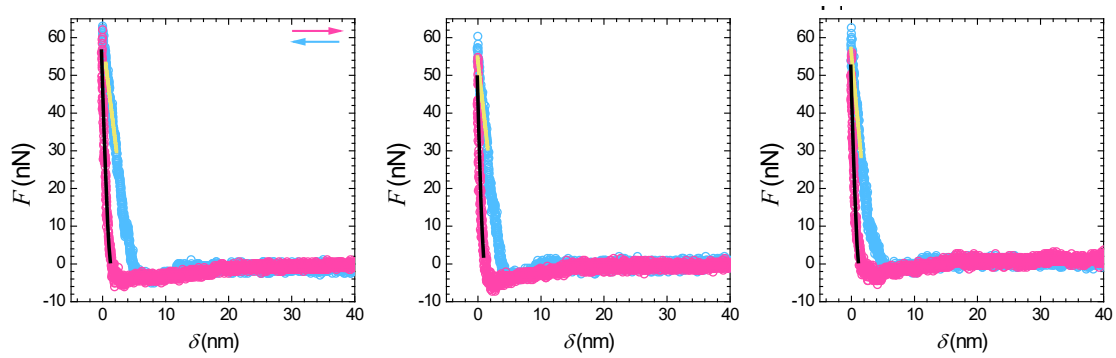


Figure 7. Force-separation curves recorded for neat PTF, PTF-LIPSS top, and PTF-LIPSS bottom. Blue circles correspond to the tip approach, while pink circles to the tip retraction.

In Figure 7, F is the force sensed by the AFM probe, and δ the so-called separation, *i.e.*, the distance between the tip and the sample (including indentation). The continuous yellow and black lines correspond to the stiffness and mechanical modulus fittings, respectively. These two properties are related to each other, being linearly proportional

in the elastic regime. However, we clarify that stiffness is a structural property that depends on sample geometry, while the mechanical modulus is an intrinsic material property. In this work, we present both values as mutually complementary. On one hand, although stiffness is an extensive property, its calculation from the force spectroscopy curves is straightforward and model independent, being very reliable. On the other hand, even if the mechanical modulus is directly related to the materials' properties, its calculation is model dependent and requires information about the probe's geometry, increasing possible error sources as recently discussed in the literature [51-53].

The stiffness, defined as $\Delta F/\Delta \delta$, was calculated by fitting the approach data (light blue circles) to an order 1 polynomial function, in the 50-90% total force range. This parameter defines the resistance opposed by the polymer surface when the AFM tip penetrates it. The Young's modulus (E_Y) of the samples was calculated using the retract curve. This value is also a measure of the sample stiffness, now calculated as the resistance oppose by the sample to probe withdrawal. In our present work, the Young's modulus (E_Y) was obtained by fitting the retract curve (pink circles in Figure 7) to the DMT model [54]:

$$F - F_{\text{adh}} = \frac{4}{3} \frac{E_Y}{(1 - \vartheta^2)} R^{1/2} \delta^{3/2} \quad (1)$$

where F_{adh} is the tip-sample adhesion force, R the tip radius, and ϑ_s^{\square} is the Poisson's ratio of PTF, taken as 0.3. The values obtained from the force-separation curves analysis are summarized in Table 3.

Table 3. Force-distance curve analysis results for PTF and PTF-LIPSS. For all parameters, we present the mean value and standard deviation, calculated for 20 random points on the samples.

	Stiffness (N/m)	E_Y (GPa)	δ_i (nm)	F_{adh} (nN)
PTF	13.5 ± 0.3	2.8 ± 0.2	5 ± 1	3 ± 1

PTF-LIPSS top	17.3 ± 0.3	3.3 ± 0.3	5 ± 1	5 ± 2
PTF-LIPSS bottom	16.2 ± 0.4	3.5 ± 0.3	5 ± 2	5 ± 3

For the non-irradiated PTF, we obtained a stiffness of 13 N/m and an E_Y of 2.8 GPa. This latter value is higher than that reported by Guidotti et al [35], using tensile test measurements, and than that reported by Klonos et al using indentation tests [36]; however, the order of magnitude is fairly comparable to both literature reports. This increase in E_Y can be understood considering that we are reporting a surface modulus value, which can be different from the bulk one. The force spectroscopy analysis performed on the top and bottom of PTF-LIPSS showed a $\sim 25\%$ increase in the stiffness values, and a concomitant increase in E_Y in about $\sim 20\%$ (as expected). These facts indicated that the top and bottom of PTF-LIPSS are harder, compared to the non-irradiated material. This observation is in line to a previous report in polymer LIPSS. In Ref [39], the authors showed that for PET films there was an E_Y increase of above 150% in the irradiated samples. This increase was related to the surface oxidation suffered by the PET during LIPSS formation. In our present work, the changes in E_Y denote that possible oxidation on the PTF surface, during LIPSS formation, should be very low. This fact supports those found by ATR-FTIR and CA measurements in the previous section. The tip indentation into the sample (δ_i) was also calculated from the force-distance curves. We observed a constant value, within statistical error, for all probed samples. This fact indicates that the PTF chains did not present any change in their compressibility after irradiation, as previously discussed for nanostructured polymer systems [55]. This discussion also supports the almost invariable value of the stiffness between samples. Finally, adhesion forces (F_{adh}) measured on the PTF-LIPSS showed a small increase, compared to the non-irradiated sample. This result is different from the one found via

nanomechanical mapping. We relate this differences to the distinct rates at which each measurement was performed (2 kHz for PF-QNM vs 1 Hz for force spectroscopy). However, we do not discard that the changes in F_{adh} could relate also to the slight changes in physicochemical properties of the material after irradiation. Taking all these facts into consideration, we determined that LIPSS on PTF allow not only the formation of a wrinkled pattern, but also tailoring the surface mechanical properties, without compromising the macroscopic physicochemical behavior.

Conclusions

We prepared wrinkled surfaces composed by periodic nanostructures, on poly(trimethylene 2,5-furanoate) free-standing films, by laser irradiation. An atomic force microscopy study showed that it was possible to develop LIPSS on PTF with only 600 laser pulses and a fluence of 8 mJ/cm². The optimal conditions were found for irradiations using 3600 pulses, with the same fluence. We evaluated the physicochemical changes taking place on the polymer surface after irradiation, using a combined macro- and nanoscale approach. The macroscopic physicochemical properties of PTF showed almost no changes after nanostructure formation. This result differed from those previously found for the terephthalic counterparts, PET and PTT, and points out the positive role that the furan ring had during laser processing. By force spectroscopy measurements, we determined that the PTF nanostructures provided the polymer with an enhanced mechanical response. In particular, we obtained a stiffer surface, as observed by the increased Young's modulus, for the nanostructured sample.

Moreover, this study highlights the possibility to reduce the whole environmental impact for polymer nanostructure production by replacing terephthalic polyesters with furan-based ones, thanks to two main reasons: i) the fully bio-based nature of PTF; ii) the

reduction of laser energy necessary for LIPSS production. In conclusion, the possibility of nanostructuring with success the PTF surface film by laser irradiation, is a result of great value, as it opens the way to new possible areas of application for furan-based polyesters, such as organic electronics and medical devices, not concretely considered so far.

Acknowledgments

This work has been supported by Ministry of Science, Innovation and Universities (MCIU, Spain) under the project CTQ2016-75880-P. D.E.M. acknowledges the financial support obtained through the Post-Doctoral fellowship “Juan de la Cierva – Incorporación” (IJCI-2017-31600, MCIU, Spain). E.R. thanks MCIU for the tenure of a Ramón y Cajal contract (No. RYC-2011-08069). Authors thank Dr. Robles-Hernández (University of the Basque Country, UPV/EHU) for assistance on force spectroscopy analysis.

References

- [1] E. Rebollar, T.A. Ezquerro, A. Nogales, Laser-Induced Periodic Surface Structures (LIPSS) on Polymer Surfaces, in: C.M. González-Henríquez, J. Rodríguez-Hernández (Eds.), *Wrinkled Polymer Surfaces: Strategies, Methods and Applications*, Springer International Publishing, Cham, 2019, pp. 143-155.
- [2] C. Mijangos, R. Hernández, J. Martín, A review on the progress of polymer nanostructures with modulated morphologies and properties, using nanoporous AAO templates, *Progress in Polymer Science* 54-55 (2016) 148-182.
- [3] M. Elsayahy, G.S. Heo, S.-M. Lim, G. Sun, K.L. Wooley, Polymeric Nanostructures for Imaging and Therapy, *Chemical Reviews* 115(19) (2015) 10967-11011.
- [4] M. Cheng, Y.-N. Meng, Z.-X. Wei, Conducting Polymer Nanostructures and their Derivatives for Flexible Supercapacitors, *Israel Journal of Chemistry* 58(12) (2018) 1299-1314.
- [5] J. Rodríguez-Hernández, Wrinkled interfaces: Taking advantage of surface instabilities to pattern polymer surfaces, *Progress in Polymer Science* 42 (2015) 1-41.
- [6] E. Rebollar, M. Castillejo, T.A. Ezquerro, Laser induced periodic surface structures on polymer films: From fundamentals to applications, *European Polymer Journal* 73 (2015) 162-174.

- [7] J. Bonse, S. Höhm, S.V. Kirner, A. Rosenfeld, J. Krüger, Laser-Induced Periodic Surface Structures— A Scientific Evergreen, *IEEE Journal of Selected Topics in Quantum Electronics* 23(3) (2017) 1.
- [8] O. Varlamova, J. Reif, S. Varlamov, M. Bestehorn, Self-organized Surface Patterns Originating from Laser-Induced Instability, in: S. Sakabe, C. Lienau, R. Grunwald (Eds.), *Progress in Nonlinear Nano-Optics*, Springer International Publishing, Cham, 2015, pp. 3-29.
- [9] D. Bäuerle, *Instabilities and Structure Formation, Laser Processing and Chemistry*, Springer Berlin Heidelberg, Berlin, Heidelberg, 2011, pp. 623-677.
- [10] M. Bolle, S. Lazare, Submicron periodic structures produced on polymer surfaces with polarized excimer laser ultraviolet radiation, *Applied Surface Science* 65-66 (1993) 349-354.
- [11] I. Martín-Fabiani, E. Rebollar, S. Pérez, D.R. Rueda, M.C. García-Gutiérrez, A. Szymczyk, Z. Roslaniec, M. Castillejo, T.A. Ezquerra, Laser-Induced Periodic Surface Structures Nanofabricated on Poly(trimethylene terephthalate) Spin-Coated Films, *Langmuir* 28(20) (2012) 7938-7945.
- [12] J. Cui, A. Nogales, T.A. Ezquerra, E. Rebollar, Influence of substrate and film thickness on polymer LIPSS formation, *Applied Surface Science* 394 (2017) 125-131.
- [13] P. Slepíčka, J. Siegel, O. Lyutakov, N. Slepíčková Kasálková, Z. Kolská, L. Bačáková, V. Švorčík, Polymer nanostructures for bioapplications induced by laser treatment, *Biotechnology Advances* 36(3) (2018) 839-855.
- [14] D. Fajstavr, K. Neznalová, V. Švorčík, P. Slepíčka, LIPSS Structures Induced on Graphene-Polystyrene Composite, *Materials* 12(21) (2019) 3460.
- [15] M. Bolle, S. Lazare, Characterization of submicrometer periodic structures produced on polymer surfaces with low-fluence ultraviolet laser radiation, *Journal of Applied Physics* 73(7) (1993) 3516-3524.
- [16] M. Csete, Z. Bor, Laser-induced periodic surface structure formation on polyethylene-terephthalate, *Applied Surface Science* 133(1) (1998) 5-16.
- [17] M. Mezera, J. Bonse, G.-w.R.B.E. Römer, Influence of Bulk Temperature on Laser-Induced Periodic Surface Structures on Polycarbonate, *Polymers* 11(12) (2019) 1947.
- [18] S.Y. Son, G. Kang, M. Kim, J. Lee, T. Kim, T. Park, J. Lim, In-depth optical characterization of poly(3-hexylthiophene) after formation of nanosecond laser-induced periodic surface structures, *Nanoscale* 11(16) (2019) 7567-7571.
- [19] E. Rebollar, I. Frischauf, M. Olbrich, T. Peterbauer, S. Hering, J. Preiner, P. Hinterdorfer, C. Romanin, J. Heitz, Proliferation of aligned mammalian cells on laser-nanostructured polystyrene, *Biomaterials* 29(12) (2008) 1796-806.
- [20] E. Rebollar, S. Pérez, M. Hernández, C. Domingo, M. Martín, T.A. Ezquerra, J.P. García-Ruiz, M. Castillejo, Physicochemical modifications accompanying UV laser induced surface structures on poly(ethylene terephthalate) and their effect on adhesion of mesenchymal cells, *Physical Chemistry Chemical Physics* 16(33) (2014) 17551-17559.
- [21] E. Rebollar, M. Sanz, S. Pérez, M. Hernández, I. Martín-Fabiani, D.R. Rueda, T.A. Ezquerra, C. Domingo, M. Castillejo, Gold coatings on polymer laser induced periodic surface structures: assessment as substrates for surface-enhanced Raman scattering, *Physical Chemistry Chemical Physics* 14(45) (2012) 15699-15705.
- [22] E. Rebollar, M. Hernández, M. Sanz, S. Pérez, T.A. Ezquerra, M. Castillejo, Laser-induced surface structures on gold-coated polymers: Influence of morphology on

surface-enhanced Raman scattering enhancement, *Journal of Applied Polymer Science* 132(45) (2015).

[23] D.E. Martínez-Tong, Á. Rodríguez-Rodríguez, A. Nogales, M.-C. García-Gutiérrez, F. Pérez-Murano, J. Llobet, T.A. Ezquerra, E. Rebollar, Laser Fabrication of Polymer Ferroelectric Nanostructures for Nonvolatile Organic Memory Devices, *ACS Applied Materials & Interfaces* 7(35) (2015) 19611-19618.

[24] Á. Rodríguez-Rodríguez, E. Rebollar, M. Soccio, T.A. Ezquerra, D.R. Rueda, J.V. Garcia-Ramos, M. Castillejo, M.-C. Garcia-Gutierrez, Laser-Induced Periodic Surface Structures on Conjugated Polymers: Poly(3-hexylthiophene), *Macromolecules* 48(12) (2015) 4024-4031.

[25] n.-l. European Bioplastics, Bioplastics market data 2018 - Global production capacities of bioplastics 2018-2023, 2018.

[26] A.F. Sousa, C. Vilela, A.C. Fonseca, M. Matos, C.S.R. Freire, G.-J.M. Gruter, J.F.J. Coelho, A.J.D. Silvestre, Biobased polyesters and other polymers from 2,5-furandicarboxylic acid: a tribute to furan excellency, *Polymer Chemistry* 6(33) (2015) 5961-5983.

[27] G.Z. Papageorgiou, D.G. Papageorgiou, Z. Terzopoulou, D.N. Bikiaris, Production of bio-based 2,5-furan dicarboxylate polyesters: Recent progress and critical aspects in their synthesis and thermal properties, *European Polymer Journal* 83 (2016) 202-229.

[28] R.-J. van Putten, J.C. van der Waal, E. de Jong, C.B. Rasrendra, H.J. Heeres, J.G. de Vries, Hydroxymethylfurfural, A Versatile Platform Chemical Made from Renewable Resources, *Chemical Reviews* 113(3) (2013) 1499-1597.

[29] S.K. Burgess, O. Karvan, J.R. Johnson, R.M. Kriegel, W.J. Koros, Oxygen sorption and transport in amorphous poly(ethylene furanoate), *Polymer* 55(18) (2014) 4748-4756.

[30] S.K. Burgess, C.R. Mubarak, R.M. Kriegel, W.J. Koros, Physical aging in amorphous poly(ethylene furanoate): Enthalpic recovery, density, and oxygen transport considerations, *Journal of Polymer Science Part B: Polymer Physics* 53(6) (2015) 389-399.

[31] S.K. Burgess, R.M. Kriegel, W.J. Koros, Carbon Dioxide Sorption and Transport in Amorphous Poly(ethylene furanoate), *Macromolecules* 48(7) (2015) 2184-2193.

[32] S.K. Burgess, D.S. Mikkilineni, D.B. Yu, D.J. Kim, C.R. Mubarak, R.M. Kriegel, W.J. Koros, Water sorption in poly(ethylene furanoate) compared to poly(ethylene terephthalate). Part 2: Kinetic sorption, *Polymer* 55(26) (2014) 6870-6882.

[33] S.K. Burgess, J.E. Leisen, B.E. Kraftschik, C.R. Mubarak, R.M. Kriegel, W.J. Koros, Chain Mobility, Thermal, and Mechanical Properties of Poly(ethylene furanoate) Compared to Poly(ethylene terephthalate), *Macromolecules* 47(4) (2014) 1383-1391.

[34] L. Genovese, N. Lotti, V. Siracusa, A. Munari, Poly(Neopentyl Glycol Furanoate): A Member of the Furan-Based Polyester Family with Smart Barrier Performances for Sustainable Food Packaging Applications, *Materials (Basel)* 10(9) (2017).

[35] G. Guidotti, M. Soccio, N. Lotti, M. Gazzano, V. Siracusa, A. Munari, Poly(propylene 2,5-thiophenedicarboxylate) vs. Poly(propylene 2,5-furandicarboxylate): Two Examples of High Gas Barrier Bio-Based Polyesters, *Polymers* 10(7) (2018) 785.

[36] P.A. Klonos, L. Papadopoulos, D. Tzetzis, A. Kyritsis, G.Z. Papageorgiou, D.N. Bikiaris, Thermal, nanoindentation and dielectric study of nanocomposites based on poly(propylene furanoate) and various inclusions, *Materials Today Communications* 20 (2019) 100585.

- [37] R.I. Rodríguez-Beltrán, S. Paszkiewicz, A. Szymczyk, Z. Rosłaniec, A. Nogales, T.A. Ezquerro, M. Castillejo, P. Moreno, E. Rebollar, Laser induced periodic surface structures on polymer nanocomposites with carbon nanoadditives, *Applied Physics A* 123(11) (2017) 717.
- [38] H. Gojzewski, J. Obszarska, A. Harlay, M.A. Hempenius, G.J. Vancso, Designer poly(urea-siloxane) microspheres with controlled modulus and size: Synthesis, morphology, and nanoscale stiffness by AFM, *Polymer* 150 (2018) 289-300.
- [39] R.I. Rodríguez-Beltrán, D.E. Martínez-Tong, A. Reyes-Contreras, S. Paszkiewicz, A. Szymczyk, T.A. Ezquerro, P. Moreno, E. Rebollar, Laterally-resolved mechanical and tribological properties of laser-structured polymer nanocomposites, *Polymer* 168 (2019) 178-184.
- [40] M. Criado, E. Rebollar, A. Nogales, T.A. Ezquerro, F. Boulmedais, C. Mijangos, R. Hernández, Quantitative Nanomechanical Properties of Multilayer Films Made of Polysaccharides through Spray Assisted Layer-by-Layer Assembly, *Biomacromolecules* 18(1) (2017) 169-177.
- [41] X. Wu, S. Shi, Z. Yu, T.P. Russell, D. Wang, AFM nanomechanical mapping and nanothermal analysis reveal enhanced crystallization at the surface of a semicrystalline polymer, *Polymer* 146 (2018) 188-195.
- [42] C.A. Amo, R. Garcia, Fundamental High-Speed Limits in Single-Molecule, Single-Cell, and Nanoscale Force Spectroscopies, *ACS Nano* 10(7) (2016) 7117-7124.
- [43] J.E. Sader, R. Borgani, C.T. Gibson, D.B. Haviland, M.J. Higgins, J.I. Kilpatrick, J. Lu, P. Mulvaney, C.J. Shearer, A.D. Slattey, P.-A. Thorén, J. Tran, H. Zhang, H. Zhang, T. Zheng, A virtual instrument to standardise the calibration of atomic force microscope cantilevers, *Review of Scientific Instruments* 87(9) (2016) 093711.
- [44] R.I. Rodríguez-Beltrán, M. Hernandez, S. Paszkiewicz, A. Szymczyk, Z. Rosłaniec, T.A. Ezquerro, M. Castillejo, P. Moreno, E. Rebollar, Laser induced periodic surface structures formation by nanosecond laser irradiation of poly (ethylene terephthalate) reinforced with Expanded Graphite, *Applied Surface Science* 436 (2018) 1193-1199.
- [45] D. Knittel, E. Schollmeyer, Surface structuring of synthetic fibres by UV laser irradiation. Part III. Surface functionality changes resulting from excimer-laser irradiation, *Polymer International* 45(1) (1998) 103-109.
- [46] R.N. Wenzel, RESISTANCE OF SOLID SURFACES TO WETTING BY WATER, *Industrial & Engineering Chemistry* 28(8) (1936) 988-994.
- [47] A.B.D. Cassie, S. Baxter, Wettability of porous surfaces, *Transactions of the Faraday Society* 40(0) (1944) 546-551.
- [48] D.K. Owens, R.C. Wendt, Estimation of the surface free energy of polymers, *Journal of Applied Polymer Science* 13(8) (1969) 1741-1747.
- [49] D.H. Kaelble, Dispersion-Polar Surface Tension Properties of Organic Solids, *The Journal of Adhesion* 2(2) (1970) 66-81.
- [50] R.J. Good, in: K.L. Mittal (Ed.), *Contact Angle Wettability and Adhesion*, VSP Press, Utrecht, The Netherlands, 1993, p. 3.
- [51] B. Pittenger, D. Yablon, Improving the Accuracy of Nanomechanical Measurements with Force-Curve-Based AFM Techniques, *Bruker Application Note #149* (2017).
- [52] S. Fujinami, E. Ueda, K. Nakajima, T. Nishi, Analytical methods to derive the elastic modulus of soft and adhesive materials from atomic force microscopy force measurements, *Journal of Polymer Science Part B: Polymer Physics* 57(18) (2019) 1279-1286.

- [53] S.V. Kontomaris, A. Malamou, Hertz model or Oliver & Pharr analysis? Tutorial regarding AFM nanoindentation experiments on biological samples, *Materials Research Express* 7(3) (2020) 033001.
- [54] B.V. Derjaguin, V.M. Muller, Y.P. Toporov, Effect of contact deformations on the adhesion of particles, *Journal of Colloid and Interface Science* 53(2) (1975) 314-326.
- [55] P.M. Claesson, I. Dobryden, G. Li, Y. He, H. Huang, P.A. Thoren, D.B. Haviland, From force curves to surface nanomechanical properties, *Phys Chem Chem Phys* 19(35) (2017) 23642-23657.